Supporting Information

Band Convergence and Carrier-density Fine-tuning as the Electronic Origin of High-average Thermoelectric Performance in Pb-doped GeTe-based Alloys

Yamei Feng[#], Junqin Li [#], Yu Li[#], Teng Ding, Chunxiao Zhang, Lipeng Hu, Fusheng Liu, Weiqin Ao and Chaohua Zhang*

College of Materials Science and Engineering, Shenzhen Key Laboratory of Special Functional Materials, Shenzhen Engineering Laboratory for Advanced Technology of Ceramics, Guangdong Research Center for Interfacial Engineering of Functional Materials, Institute of Deep Underground Sciences and Green Energy, Shenzhen University, Shenzhen 518060, China

[#] Author contributed equally to this work

*Corresponding author, E-mail: zhangch@szu.edu.cn

Supporting methods for the theoretical modeling

1. Parabolic two-band model for electrical transport

The primary valence band *L* and secondary valence band *H* with an energy difference ΔE_{L-H} (from 0.14 to 0.06 eV) are considered in this parabolic two-band model. Reference to previous literatures,[1, 2] we set the effective mass of the band *L* (m_L^*) and band *H* (m_H^*) as 1.2 m_e and 6.1 m_e respectively in our theoretical modeling. The Seebeck coefficient S_L for the band *L* is calculated as below:[3]

$$S_L = \frac{k_B}{e}\left[\frac{(r+2.5)F_{r+1.5}(E_F^*)}{(r+1.5)F_{r+0.5}(E_F^*)} - E_F^*\right] \quad (1)$$

where k_B is the Boltzmann constant, e is electron charge, E_F^* is the reduced Fermi level $\frac{E_F}{k_B T}$, r is the scattering parameters (generally set $r = -0.5$ for acoustic scattering), and the general Fermi integrals F_s is defined as:[3]

$$F_s(E_F^*) = \int_0^\infty \frac{E^{*s}}{1+exp(E^*-E_F^*)} dE^* \quad (2)$$

The light-hole carrier density p_L of band *L* is set as:[3]

$$p_L = \frac{1}{2\pi^2}\left(\frac{2m_L^* k_B T}{\hbar^2}\right)^{3/2} F_{0.5}(E_F^*) \quad (3)$$

The electrical conductivity σ_L of band *L* is set as:[3]

$$\sigma_L = \frac{e^2\tau_0}{3\pi^2 m_L^*}(r+1.5)\left(\frac{2m_L^* k_B T}{\hbar^2}\right)^{3/2} F_{r+0.5}(E_F^*) \quad (4)$$

The corresponding Seebeck coefficient S_H, carrier density p_H and electrical conductivity σ_H for the *H* band can be calculated as below:

$$S_H = \frac{k_B}{e}\left[\frac{(r+2.5)F_{r+1.5}(E_F^*-\Delta)}{(r+1.5)F_{r+0.5}(E_F^*-\Delta)} - (E_F^*-\Delta)\right] \quad (5)$$

$$p_H = \frac{1}{2\pi^2}\left(\frac{2m_H^* k_B T}{\hbar^2}\right)^{3/2} F_{0.5}(E_F^*-\Delta) \quad (6)$$

$$\sigma_H = \frac{e^2\tau_0}{3\pi^2 m_H^*}(r+1.5)\left(\frac{2m_H^* k_B T}{\hbar^2}\right)^{3/2} F_{r+0.5}(E_F^*-\Delta) \quad (7)$$

where Δ represent the reduced energy difference $\frac{\Delta E_{L-H}}{k_B T}$. Approximately, we take the scattering time τ_0 as a constant in the theoretical modelling of *S*.

The total Seebeck coefficient is calculated as:

$$S_{total} = (\sigma_L S_L + \sigma_H S_H)/(\sigma_L + \sigma_H) \quad (8)$$

The measured total Hall carrier concentration p_{Hall} for the two-band model is given as: [4]

$$p_{Hall} = (\mu_L p_L + \mu_H p_H)^2/(A_L {\mu_L}^2 p_L + A_H {\mu_H}^2 p_H) \quad (9)$$

where $A_{L,H}$ and $\mu_{L,H}$ are the Hall factor and carrier mobility, respectively. The Hall factor $A_{L,H}$ usually lies in the range of 1-2, and the theoretical $A_{L,H}$ is calculated to be ~1.18 when only considering the acoustic scattering.[4] Not that the measured Hall carrier concentration p_{Hall} is smaller than the actual total hole concentration $p_{total} = p_L + p_H$.

For the modeling of the carrier-density-dependent power factor *PF* and figure of merit *ZT*, the experimental data of carrier mobility μ_{exp} and lattice thermal conductivity κ_{lat} are used in the theoretical computing. The carrier thermal conductivity κ_e is calculated by the $\kappa_e = LT/\rho$, where the Lorenz number L is estimated by an empirical equation:[5] $L = 1.5 + \exp(-|S|/116)$ (S and L are in the unit of μVK^{-1} and 10^{-8} WΩK^{-2} respectively). The total thermal conductivity κ_{tot} is the sum of κ_e and κ_{lat}.

2. Parabolic three-band model for electrical transport

In order to consider the bipolar transport at higher temperatures, the three-band model including a conduction band is used for the theoretical modeling. Reference to previous literatures,[1, 2] the effective mass of the conduction band *C* (m_c^*) of GeTe is estimated to be 0.78 m_e, and the bandgap E_g is about 0.23 eV based on the results of first-principle calculations.

The corresponding Seebeck coefficient S_c, carrier density n_c and electrical conductivity σ_c of the conduction band are listed below:

$$S_c = -\frac{k_B}{e}\left[\frac{(r+2.5)F_{r+1.5}(-E_F^*-\delta)}{(r+1.5)F_{r+0.5}(-E_F^*-\delta)} - (-E_F^* - \delta)\right] \quad (10)$$

$$n_c = \frac{1}{2\pi^2}\left(\frac{2m_c^* k_B T}{\hbar^2}\right)^{3/2} F_{0.5}(-E_F^* - \delta) \quad (11)$$

$$\sigma_c = \frac{e^2\tau_0}{3\pi^2 m_c^*}(r+1.5)\left(\frac{2m_c^* k_B T}{\hbar^2}\right)^{\frac{3}{2}} F_{r+0.5}(-E_F^* - \delta) \quad (12)$$

where δ represent the reduced band gap $\frac{E_g}{k_B T}$.

The total Seebeck coefficient in the three-band model is calculated as:

$$S_{total} = (\sigma_L S_L + \sigma_H S_H + \sigma_c S_c)/(\sigma_L + \sigma_H + \sigma_c) \quad (13)$$

In the theoretical modelling process, the Fermi level is first determined by the measured room-temperature Hall concentration, then the actual total hole concentration at 300 K is determined by $p_{total} = p_L + p_H = p_0$. As revealed by the temperature-dependent Hall measurement (Figure S1), the measured Hall carrier concentration p_{Hall} first stays as a constant and then exponentially increases with the temperature. Therefore, we use a constant carrier density p_0 from 300 to 500 K and a varying carrier density $p_0 exp(A - \frac{B}{T})$ from 500 to 800 K to model the temperature-dependent carrier density. Because the electron concentration n_c comes from the intrinsic excitation, knowing $n_c = n_{bi} = p_{bi}$, we then have $p_L + p_H - n_c$ equals to p_0 from 300 to 500 K and $p_0 exp(A - \frac{B}{T})$ from 500 to 800 K.

3. Debye-Callaway model for calculating the lattice thermal conductivity:

The temperature (T)-dependent $\kappa_{lat}(T)$ can be expressed as a sum of the spectral lattice thermal conductivity $\kappa_s(\omega)$ from different frequencies using the Debye-Callaway model: [6, 7]

$$\kappa_{lat} = \int \kappa_s(\omega)\, d\omega = \frac{1}{3}\int_0^{\omega_a} C_s(\omega) v_g(\omega)^2 \tau_{tot}(\omega) d\omega \quad (14)$$

Thus, the $\kappa_s(\omega)$ is determined by the $C_s(\omega)$, the frequency-dependent phonon group velocity $v_g(\omega)$ and total relaxation time $\tau_{tot}(\omega)$. Generally, as the phonons in optical branches shows low velocity, only the phonons in acoustic branches are considered to calculate the κ_{lat}. Thus, the cut-off frequency for acoustic branches ω_a is given by $\omega_a = (\frac{6\pi^2}{V_{cell}})^{1/3} v_s = (\frac{6\pi^2}{NV_{av}})^{1/3} v_s$, where N, V_{av} and v_s are the atomic

numbers in a primitive cell, average atomic volume and sound speed respectively. For simple approximation, the frequency-dependent phonon group velocity $v_g(\omega)$ is set as a constant value v_s, and κ_{lat} is calculated by the following equation : [6, 7]

$$\kappa_{lat} = \frac{k_B}{2\pi^2 v_s}\left(\frac{k_B T}{\hbar}\right)^3 \int_0^{\theta_a/T} \tau_{tot}(x) \frac{x^4 e^x}{(e^x-1)^2} dx \quad (15)$$

The dimensionless variable *x* in equation (15) is defined as x= $\hbar\omega/k_B T$, where ω is the phonon frequency and the cut-off Debye temperature for acoustic branches θ_a is given by the following equation:

$$\theta_a = \hbar\omega_a/k_B = \left(\frac{6\pi^2}{NV_{av}}\right)^{1/3}\hbar v_s/k_B. \quad (16)$$

The N=2 for the GeTe is used for the calculation of θ_a. The $\tau_{tot}(x)$ is the reciprocal sum of the relaxation times from different scattering mechanisms according to the Matthiessen's rule:[8]

$$\tau_{tot}{}^{-1} = \tau_U{}^{-1} + \tau_N{}^{-1} + \tau_{PD}{}^{-1} + \tau_B{}^{-1} + \tau_{SF}{}^{-1} + \cdots \quad (17)$$

where $\tau_U{}^{-1}$, $\tau_N{}^{-1}$, $\tau_{PD}{}^{-1}$, $\tau_B{}^{-1}$ and $\tau_{SF}{}^{-1}$ are the contributions from the *Umklapp* phonon-phonon scattering, normal phonon-phonon scattering, point-defect scattering, boundary scattering and stacking default scattering respectively. The $\tau_U{}^{-1}$ is calculated from the following equation: [9-11]

$$\tau_U{}^{-1} = \frac{2}{(6\pi^2)^{1/3}}\frac{k_B V_{av}{}^{1/3}\gamma^2 T}{M_{av} v_s{}^3}\omega^2 exp\left(-\frac{\theta_a}{bT}\right) = \frac{2}{(6\pi^2)^{1/3}}\frac{k_B{}^3 V_{av}{}^{1/3}\gamma^2 T^3}{M_{av} v_s{}^3 \hbar^2}x^2 exp\left(-\frac{\theta_a}{bT}\right) \quad (18)$$

where M_{av} and γ are the average atomic mass and Grüneisen parameter respectively, and *b* is a constant characteristic of the vibrational spectrum of the material. For simple approximation, the structure of $\tau_N{}^{-1}$ is set as the same as $\tau_U{}^{-1}$ with an additional factor B_N.[7, 11, 12]

$$\tau_N{}^{-1} = B_N \tau_U{}^{-1} \quad (19)$$

The $\tau_{PD}{}^{-1}$ is calculated from the following equation:[6]

$$\tau_{PD}{}^{-1} = \frac{V_{av}\Gamma}{4\pi v_s{}^3}\omega^4 = \frac{V_{av}\Gamma}{4\pi v_s{}^3}\left(\frac{k_B T}{\hbar}\right)^4 x^4 \quad (20)$$

The parameter Γ describes the mass and atomic size contrast with the lattice, which is calculated by the following equations:[9, 13-16]

$$\Gamma = \Gamma_M + \Gamma_S \tag{21}$$

$$\Gamma_M = \sum_i c_i (\frac{\bar{M}_i}{\bar{\bar{M}}})^2 \Gamma_{i,M} \quad ; \quad \Gamma_S = \sum_i c_i (\frac{\bar{r}_i}{\bar{\bar{r}}})^2 \Gamma_{i,S} \tag{22}$$

$$\Gamma_{i,M} = \sum_j f_j (1 - \frac{m_j^i}{\bar{M}_i})^2 \quad ; \quad \Gamma_{i,S} = \sum_j f_j (1 - \frac{r_j^i}{\bar{r}_i})^2 \tag{23}$$

where $\Gamma_{i,M}$ ($\Gamma_{i,S}$), c_i, $\bar{M}_i$ ($\bar{r}_i$) is mass (strain) fluctuation scattering parameters, relative fraction and average mass (atomic size) for the *i*th sublattice respectively, and $\bar{\bar{M}}$ ($\bar{\bar{r}}$) is the average atomic mass (size) of the compound from all sublattices. The m_j^i (r_j^i) and f_j represents the *j*th atomic mass (size) and atomic fraction on the he *i*th sublattice respectively.

The boundary scattering for ${\tau_B}^{-1}$ in polycrystalline materials with average grain size D can be calculated by the following equation:[6]

$${\tau_B}^{-1} = \frac{v_s}{D} \tag{24}$$

The ${\tau_{SF}}^{-1}$ is calculated by the following equation:[17]

$${\tau_{SF}}^{-1} = 0.7 \frac{{a_{lat}}^2 \gamma^2 N_s}{v_s} \omega^2 = 0.7 (\frac{k_B T}{\hbar})^2 \frac{{a_{lat}}^2 \gamma^2 N_s}{v_s} x^2 \tag{25}$$

where N_s is the number of stacking faults a line of unit length, and a_{lat} is the average lattice parameter.

Supplementary Tables and Figures

Table S1: Parameters for modelling the lattice thermal conductivity of the $Ge_{0.96(1-x)}Pb_{0.96x}Bi_{0.08}Te_{1.08}$

Parameters	Description	GeTe	x=0	x=0.15	Reference
v_s (ms^{-1})	Average velocity	1971.4	2141.1	1946.8	Measured
v_l (ms^{-1})	Longitudinal velocity	3395.6	3325.5	3200	Measured
v_t (ms^{-1})	Transverse velocity	1761.4	1929.4	1745.5	Measured
θ_a (K)	Acoustic Debye temperature	155.1	168.0	152.8	Calculated
V_{av} (10^{-29} m^3)	Average atomic volume	2.708	2.73	2.73	This work
M_{av} (10^{-25} kg)	Average atomic mass	1.66	1.757	1.909	Calculated
B_N	Ratio of normal process	0.3	0.3	0.3	fitted
γ	Grüneisen parameter	2.19	2.19	2.19	[18]
b	Characteristic of vibrational spectrum	0.9	0.9	0.9	fitted
D (μm)	Grain size	2	2	2	This work
Γ	Scattering parameter	0	0.0593	0.121	This work
a_{lat} (nm)	Lattice parameters	0.600	0.600	0.608	Calculated
N_s (10^6 m^{-1})	Number of stacking faults	0	7.5	9	This work

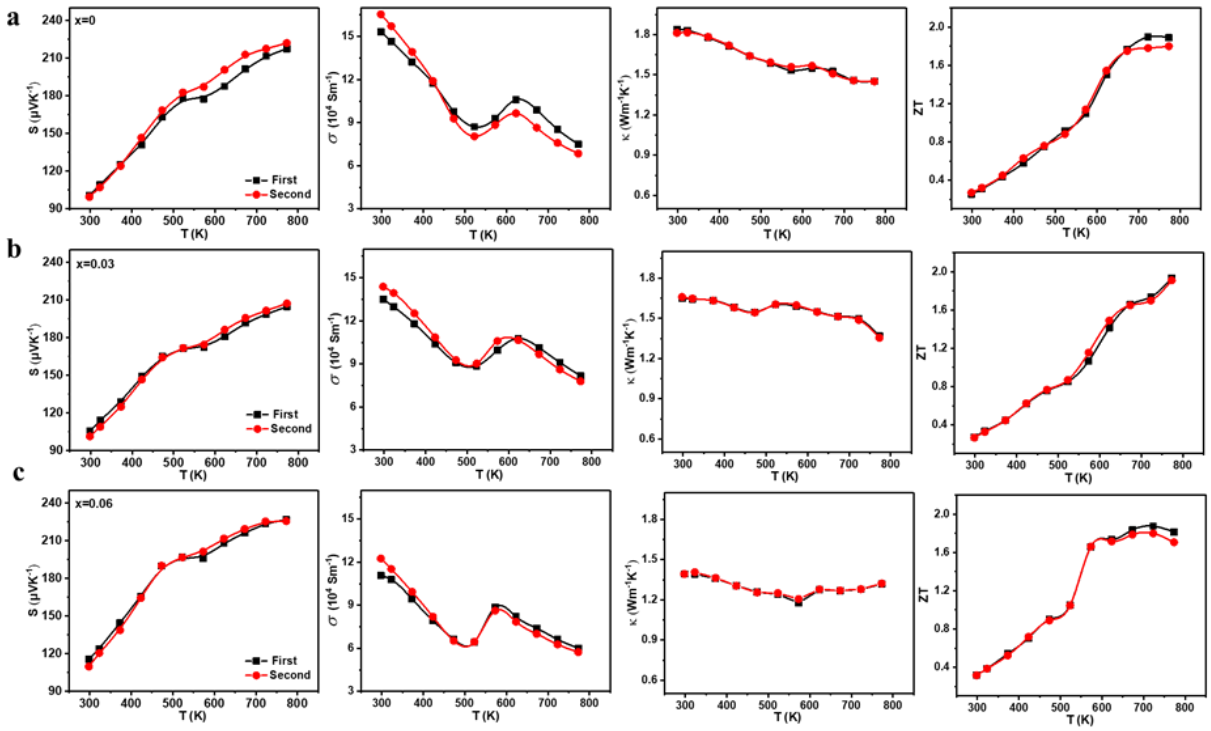

Figures S1. Repeatability test of the $Ge_{0.96(1-x)}Pb_{0.96x}Bi_{0.08}Te_{1.08}$ samples with **a)** x=0, **b)** x=0.03, **c)** x=0.06.

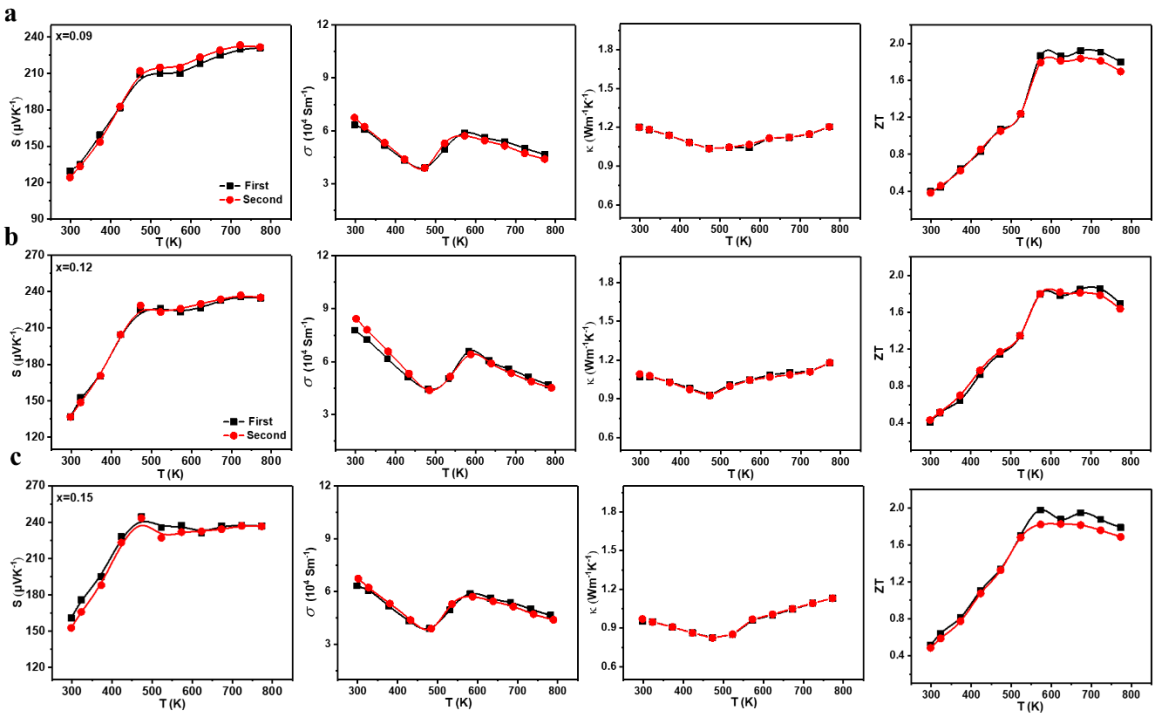

Figures S2. Repeatability test of the $Ge_{0.96(1-x)}Pb_{0.96x}Bi_{0.08}Te_{1.08}$ samples with **a)** x=0.09, **b)** x=0.12, **c)** x=0.15.

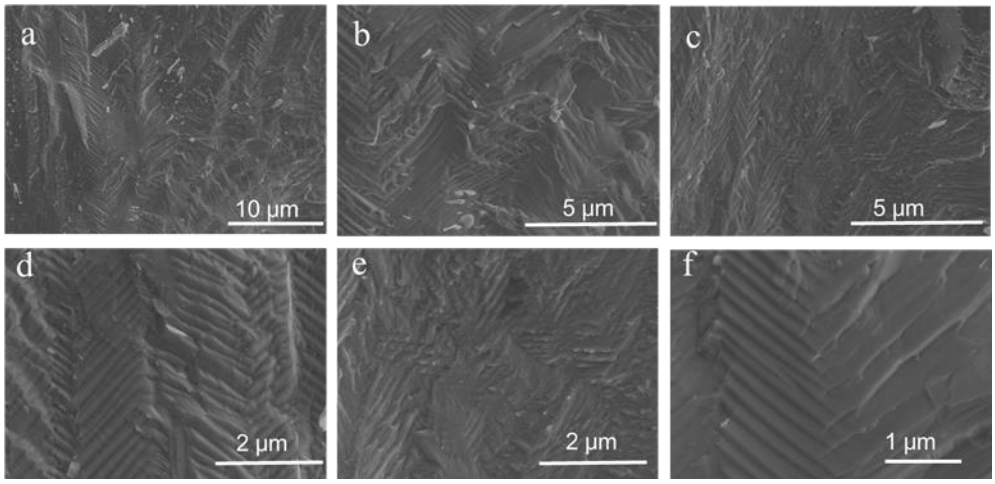

Figure S3. Microstructural characterizations of $Ge_{0.96(1-x)}Pb_{0.96x}Bi_{0.08}Te_{1.08}$ with x=0.15. (a-f) SEM image on a fractured surface.

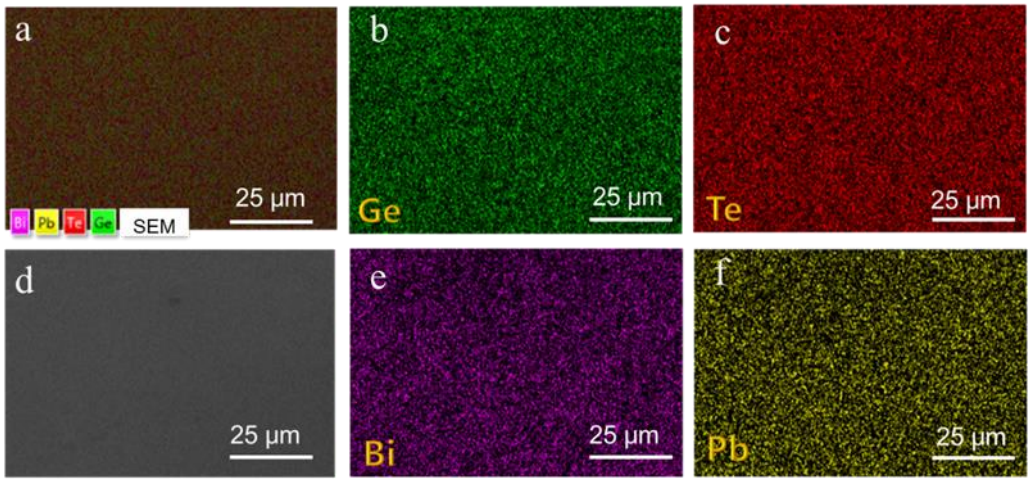

Figure S4. Microstructural characterizations of $Ge_{0.96(1-x)}Pb_{0.96x}Bi_{0.08}Te_{1.08}$ with x=0.15. **(a)** The total EDS elemental mapping. **(d)** The corresponding SEM image of the region for EDS elemental mapping. Elemental mapping graph of **(b)** Ge, **(c)** Te, **(e)** Bi and **(f)** Pb in the region as shown in **(d)**.

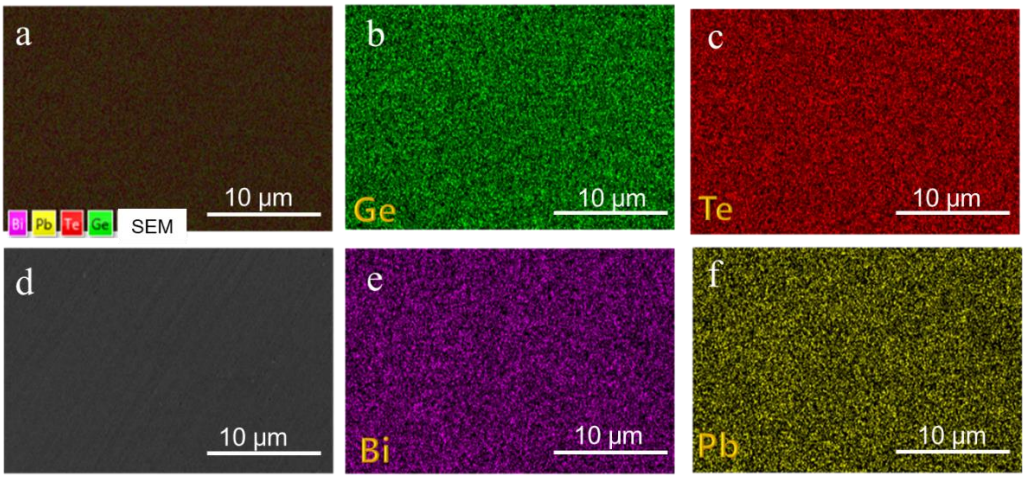

Figure S5. Microstructural characterizations of $Ge_{0.96(1-x)}Pb_{0.96x}Bi_{0.08}Te_{1.08}$ with x=0.15. **(a)** The total EDS elemental mapping. **(d)** The corresponding SEM image of the region for EDS elemental mapping. Elemental mapping graph of **(b)** Ge, **(c)** Te, **(e)** Bi and **(f)** Pb in the region as shown in **(d)**.

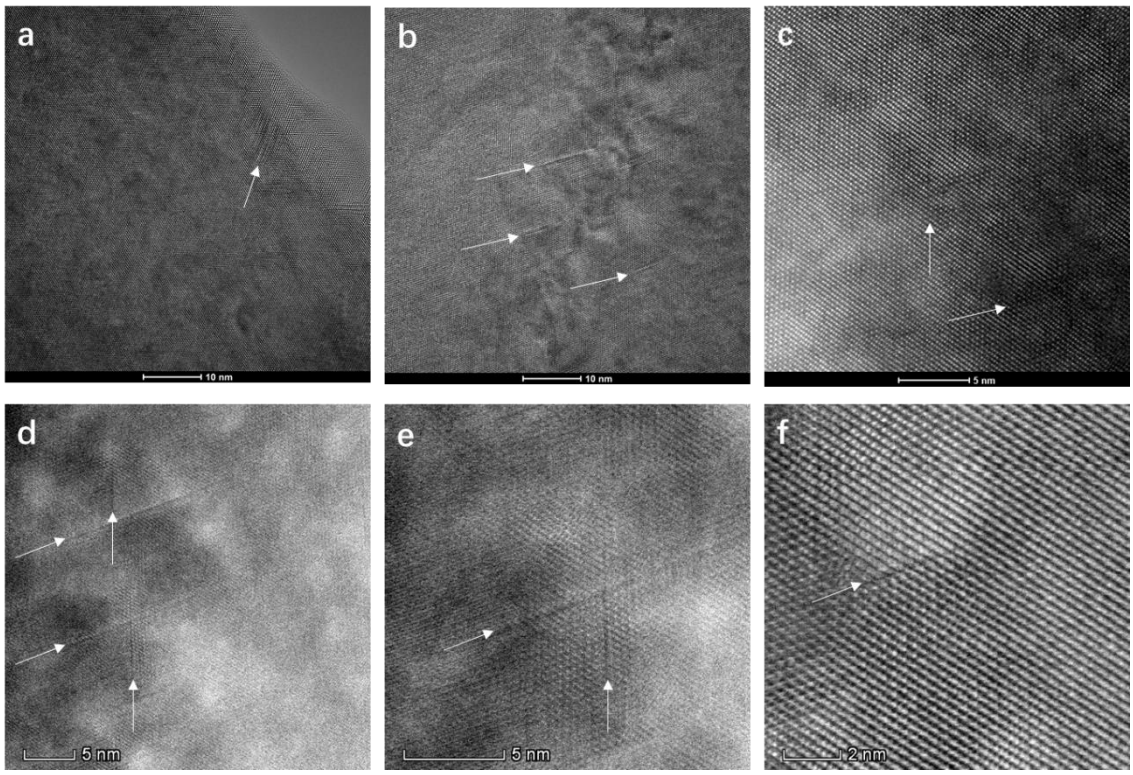

Figure S6. Transmission electron microscopy (TEM, FEI Titan G2-300) characterizations. **(a)-(c)** High-resolution scanning TEM images in different magnification. **(d)-(f)** High-angle annular dark field (HAADF) scanning TEM images in different magnification. Randomly distributed streaks or defect layers are indicated in these images, which should be ascribed to the frequently observed Ge-vacancy layers in GeTe-based alloys. These TEM images were taken on the $Ge_{0.95(1-x)}Pb_{0.95x}Bi_{0.1}Te_{1.1}$ samples with x=0.13, which have similar compositions with the $Ge_{0.96(1-x)}Pb_{0.96x}Bi_{0.08}Te_{1.08}$ samples studied in these work. More similar patterns of streaks or defect layers can also be found in our previous studied GeTe-based samples.[19]

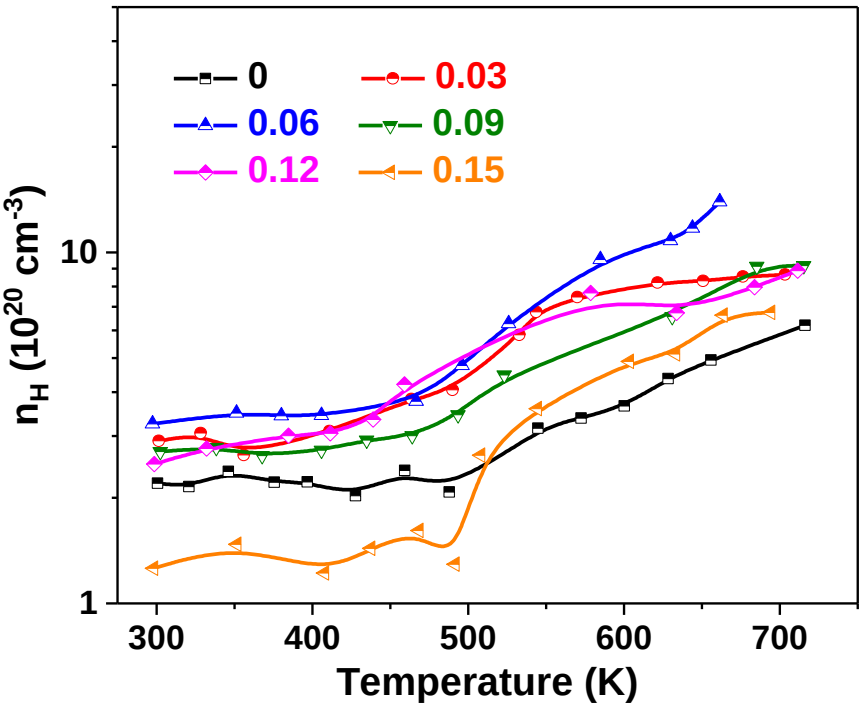

Figure S7. Temperature-dependent Hall carrier density of the $Ge_{0.96(1-x)}Pb_{0.96x}Bi_{0.08}Te_{1.08}$ samples using a customized Hall Measurement Systems, revealing that the Hall carrier density is nearly temperature-independent below 500 K but exponentially increase above 500 K.

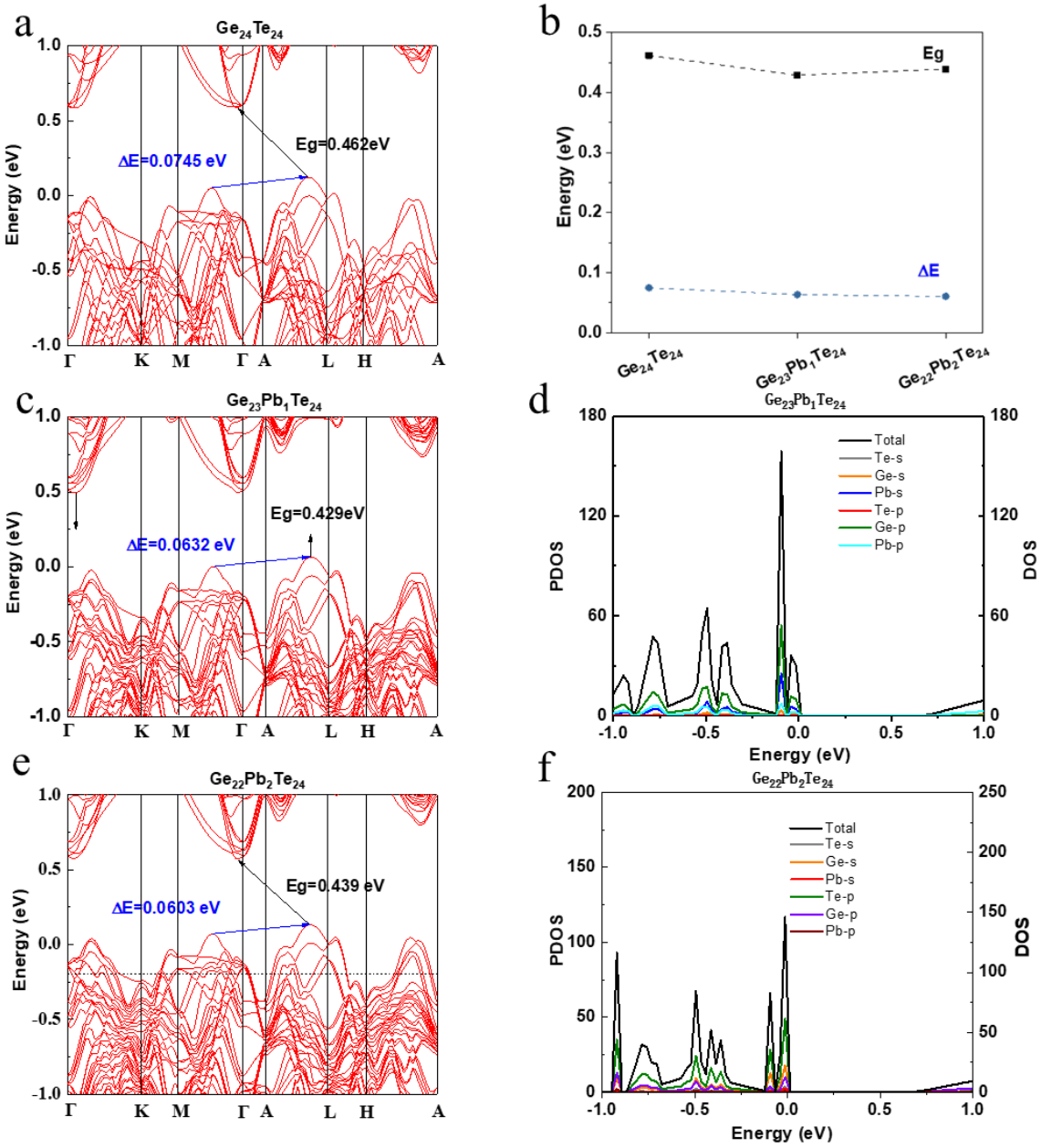

Figure S8. The DFT calculations using the rhombohedral GeTe supercell model. **a)** Band structures of the $Ge_{24}Te_{24}$. **b)** The calculated band gap E_g and the energy difference between the primary and secondary valence band ΔE_{L-H} for the $Ge_{24}Te_{24}$, $Ge_{23}Pb_1Te_{24}$, and $Ge_{22}Pb_2Te_{24}$. **c)** Band structures and **d)** DOS of the $Ge_{23}Pb_1Te_{24}$. **e)** Band structures and **f)** DOS of the $Ge_{22}Pb_2Te_{24}$.

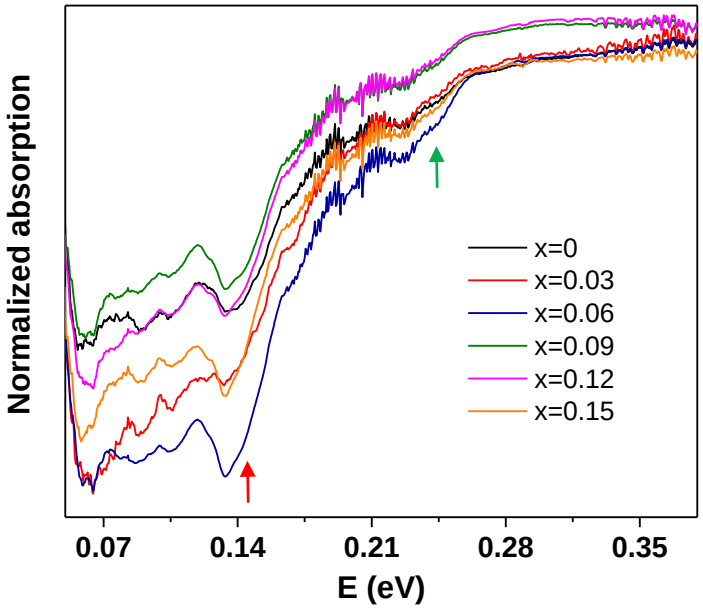

Figure S9. The infrared absorption spectrum of the $Ge_{0.96(1-x)}Pb_{0.96x}Bi_{0.08}Te_{1.08}$, revealing the optical bandgap around 0.14 eV and the existence of two kinds of valence bands with energy difference around 0.1 eV.

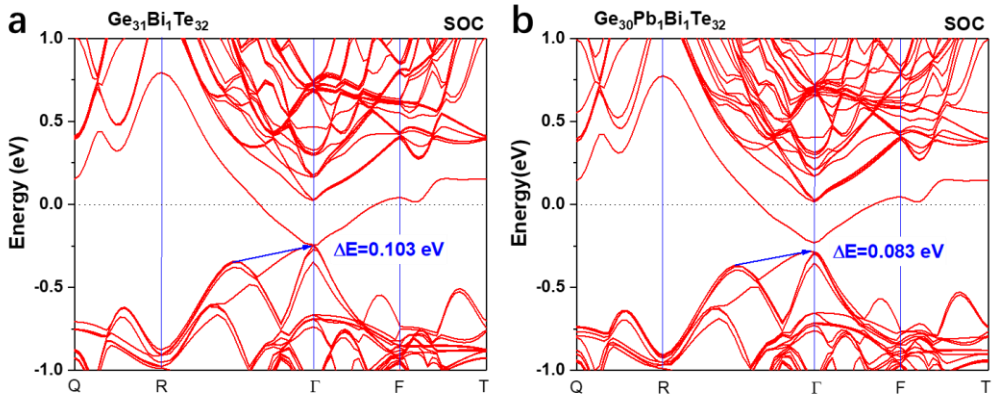

Figure S10. DFT calculated band structures of **(a)** the Bi-doped samples ($Ge_{31}Bi_1Te_{32}$) and **(b)** Pb-Bi co-doped samples ($Ge_{30}Bi_1Pb_1Te_{32}$). Impurity-induced bands associated with the trivalent Bi dopants can be found between the bandgap, which are split off from the conduction-band bottom with large shifts towards the valence-band top. More analysis about the trivalent impurity-induced bands in GeTe can also be found in other reports.[20]

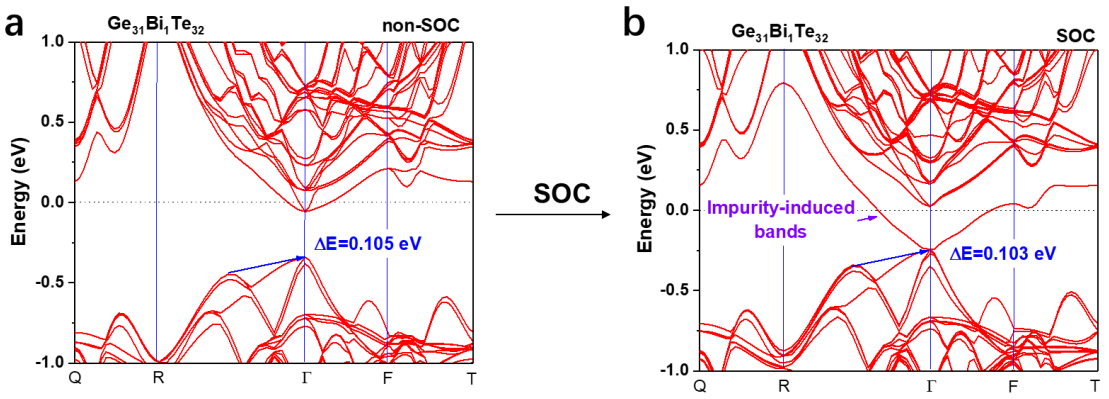

Figure S11. DFT calculated band structures of the Bi-doped samples ($Ge_{31}Bi_1Te_{32}$) **(a)** without and **(b)** with considering the spin-orbital-coupling (SOC) effect, which is the reason for the band spit of the impurity-induced band structures.

References:

1. J. E. Lewis, *Phys. Status Solidi B* 1973, **59**, 367-377.
2. D. Wu, L. D. Zhao, S. Hao, Q. Jiang, F. Zheng, J. W. Doak, H. Wu, H. Chi, Y. Gelbstein, C. Uher, C. Wolverton, M. Kanatzidis and J. He, *J. Am. Chem. Soc.*, 2014, **136**, 11412-11419.
3. H. Lee, in *Thermoelectrics: Design and Materials*, ed. H. Lee, John Wiley & Sons Ltd, 2017, DOI: 10.1002/9781118848944.ch12, pp. 206-229.
4. S. M. S. K. K. Ng, *Physics of Semiconductor Devices*, Wiley-Interscience, 2006.
5. H.-S. Kim, Z. M. Gibbs, Y. Tang, H. Wang and G. J. Snyder, *APL Mater.*, 2015, **3**, 041506.
6. J. Callaway and H. C. von Baeyer, *Phys. Rev.*, 1960, **120**, 1149-1154.
7. J. He, S. N. Girard, M. G. Kanatzidis and V. P. Dravid, *Adv. Funct. Mater.*, 2010, **20**, 764-772.
8. B. K. Agrawal and G. S. Verma, *Phys. Rev.*, 1962, **126**, 24-29.
9. D. T. Morelli, J. P. Heremans and G. A. Slack, *Physical Review B*, 2002, **66**.
10. G. A. Slack and S. Galginaitis, *Physical Review*, 1964, **133**, A253-A268.
11. J. Callaway, *Phys. Rev.*, 1959, **113**, 1046-1051.
12. E. F. Steigmeier and B. Abeles, *Physical Review*, 1964, **136**, A1149-A1155.
13. M. G. Holland, *Physical Review*, 1964, **134**, A471-A480.
14. G. A. Slack, *Physical Review*, 1962, **126**, 427-441.
15. J. Yang, G. P. Meisner and L. Chen, *Applied Physics Letters*, 2004, **85**, 1140-1142.
16. G. P. Meisner, D. T. Morelli, S. Hu, J. Yang and C. Uher, *Physical Review Letters*, 1998, **80**, 3551-3554.
17. B. K. Singh, V. J. Menon and K. C. Sood, *Phys. Rev. B*, 2006, **74**, 184302.
18. Y. Gelbstein, J. Davidow, E. Leshem, O. Pinshow and S. Moisa, *Phys. Status Solidi B* 2014, **251**, 1431-1437.
19. J. Li, Y. Xie, C. Zhang, K. Ma, F. Liu, W. Ao, Y. Li and C. Zhang, *ACS Appl. Mater. Interfaces*, 2019, **11**, 20064-20072.
20. K. Hoang, S. D. Mahanti and M. G. Kanatzidis, *Physical Review B*, 2010, **81**, 115106.